NeuroImage 244 (2021) 118574

Contents lists available at ScienceDirect

NeuroImage

journal homepage: www.elsevier.com/locate/neuroimage

Complementing canonical fMRI with functional Quantitative Susceptibility Mapping (fQSM) in modern neuroimaging research

Marta Lancione[a,b,*], Mauro Costagli[c,d], Giacomo Handjaras[e], Michela Tosetti[b,c], Emiliano Ricciardi[a], Pietro Pietrini[a], Luca Cecchetti[e]

[a] MoMiLab, IMT School for Advanced Studies Lucca, Piazza San Francesco, 19, Lucca 55100, Italy
[b] IMAGO7 Foundation, Pisa, Italy
[c] Laboratory of Medical Physics and Magnetic Resonance, IRCCS Fondazione Stella Maris, Pisa, Italy
[d] Department of Neuroscience, Rehabilitation, Ophthalmology, Genetics, Maternal and Child Sciences (DINOGMI), University of Genoa, Genoa, Italy
[e] Social and Affective Neuroscience (SANe) Group, MoMiLab, IMT School for Advanced Studies Lucca, Lucca, Italy

ARTICLE INFO

Keywords:
Quantitative Susceptibility Mapping
Functional QSM
fMRI
Spatial specificity
Quantitative BOLD
Tonotopic mapping

ABSTRACT

Functional Quantitative Susceptibility Mapping (fQSM) allows for the quantitative measurement of time-varying magnetic susceptibility across cortical and subcortical brain structures with a potentially higher spatial specificity than conventional fMRI. While the usefulness of fQSM with General Linear Model and "On/Off" paradigms has been assessed, little is known about the potential applications and limitations of this technique in more sophisticated experimental paradigms and analyses, such as those currently used in modern neuroimaging.

To thoroughly characterize fQSM activations, here we used 7T MRI, tonotopic mapping, as well as univariate (i.e., GLM and population Receptive Field) and multivariate (Representational Similarity Analysis; RSA) analyses.

Although fQSM detected less tone-responsive voxels than fMRI, they were more consistently localized in gray matter. Also, the majority of active gray matter voxels exhibited negative fQSM response, signaling the expected oxyhemoglobin increase, whereas positive fQSM activations were mainly in white matter. Though fMRI- and fQSM-based tonotopic maps were overall comparable, the representation of frequency tunings in tone-sensitive regions was significantly more balanced for fQSM. Lastly, RSA revealed that frequency information from the auditory cortex could be successfully retrieved by using either methods.

Overall, fQSM produces complementary results to conventional fMRI, as it captures small-scale variations in the activation pattern which inform multivariate measures. Although positive fQSM responses deserve further investigation, they do not impair the interpretation of contrasts of interest. The quantitative nature of fQSM, its spatial specificity and the possibility to simultaneously acquire canonical fMRI support the use of this technique for longitudinal and multicentric studies and pre-surgical mapping.

1. Introduction

Quantitative Susceptibility Mapping (QSM) (de Rochefort et al., 2010; Deistung et al., 2016; Haacke et al., 2015; Liu et al., 2015; Reichenbach et al., 2015; Shmueli et al., 2009; Wang and Liu, 2015) is a well-established method based on the phase of the Magnetic Resonance (MR) signal acquired via a Gradient Recalled Echo (GRE) sequence, which allows the non-invasive quantification of tissue magnetic susceptibility (χ). Since susceptibility represents an important biomarker for the quantitative evaluation of iron loads (Langkammer et al., 2012), myelination (Argyridis et al., 2013; Liu et al., 2011), hemorrhages and calcification (Chen et al., 2014; Deistung et al., 2013; Schweser et al., 2010; Sun et al., 2018), its employment is particularly growing in clinical studies focusing on the diagnosis and follow-up of neurodegenerative diseases, such as Parkinson's disease (Acosta-Cabronero et al., 2017; Langkammer et al., 2016; Lotfipour et al., 2012; Mazzucchi et al., 2019; Sjöström et al., 2017), multiple sclerosis (Langkammer et al., 2013; Wisnieff et al., 2015; Zhang et al., 2016), amyotrophic lateral sclerosis (Costagli et al., 2016; Donatelli et al., 2019) and Alzheimer's disease (Acosta-Cabronero et al., 2013; O'Callaghan et al., 2017). Information provided by QSM is not only quantitative, but also reflects a local property of the tissues, as free from the non-local dipole effect created by susceptibility sources that instead affect T2*-weighted images.

QSM has been recently applied to functional MRI, as well (i.e., functional QSM - fQSM) (Balla et al., 2014; Bianciardi et al., 2014; Chen et al., 2013; Chen and Calhoun, 2015; Costagli et al., 2019;

* Corresponding author at: MoMiLab, IMT School for Advanced Studies Lucca, Piazza San Francesco, 19, Lucca 55100, Italy.
E-mail address: marta.lancione@imtlucca.it (M. Lancione).

https://doi.org/10.1016/j.neuroimage.2021.118574.
Received 13 May 2021; Received in revised form 3 September 2021; Accepted 7 September 2021
Available online 8 September 2021.

Özbay et al., 2016; Shih et al., 2021; Sun et al., 2016). This method relies on the acquisition of a complex-valued GRE-EPI signal (i.e., the simultaneous acquisition of both signal magnitude and phase) (Sun and Wilman, 2015), with no increase in acquisition time. By removing the non-local dipole effect, fQSM guarantees a more direct measure of the susceptibility variation, which is responsible for the Blood Oxygenation Level-Dependent (BOLD) effect. Hence, fQSM can provide a quantitative and spatially specific correlate of neural activity.

Previous studies assessed the feasibility of fQSM (Bianciardi et al., 2014; Chen et al., 2013) and highlighted some of its characteristics. In particular, fQSM has sufficient sensitivity-though lower than magnitude-based fMRI-to detect parenchymal activation (Balla et al., 2014; Bianciardi et al., 2014). This lower sensitivity is balanced by higher spatial specificity due to the removal of the non-local dipole field effect (Balla et al., 2014; Costagli et al., 2019; Shih et al., 2021). A potentially interesting but still unclear property of fQSM is related to the sign of the activation (Balla et al., 2014; Costagli et al., 2019; Özbay et al., 2016). The net effect of the variation of the cerebral metabolic rate of oxygen and of cerebral blood flow and volume observed during neuronal activation determines a local increase of oxygenated blood in task-sensitive regions. As deoxy-hemoglobin is paramagnetic (i.e., it has positive susceptibility) and oxy-hemoglobin is diamagnetic (i.e., it has negative susceptibility), during task periods we observe a decrease in tissue susceptibility which leads to an increase in the $T2^*$-weighted signal. Hence, in voxels showing a BOLD fMRI signal increase, a negative fQSM activation is expected. Although this is the case for the vast majority, some voxels show the same directionality in BOLD fMRI and fQSM signal change. Indeed, the presence of both positive and negative fQSM activations complicates the interpretation of contrasts of interest in task-based paradigms. Unexpected directionality in fQSM could be caused by incomplete dipole inversion (Balla et al., 2014; Özbay et al., 2016), especially near strong susceptibility sources, such as veins. However, this effect has been observed using a broad range of acquisition parameters and several reconstruction algorithms, suggesting that data processing has a limited impact on this. Therefore, new studies are needed to better clarify the biophysical principles that could explain task-related fQSM signal increments.

Previous works focused on the application of conventional analysis techniques to fQSM data, such as General Linear Model (GLM) for simple task-based “On/Off” experiments. Yet, GLM is not the only approach adopted by the neuroimaging community, and more advanced tools, namely multivariate methods, have become increasingly popular in neuroscientific analytical pipelines. Also, to precisely dissect complex cognitive and affective human abilities, simple “On/Off” task designs have been replaced by paradigms including several experimental conditions. Notwithstanding progress in functional neuroimaging data analysis and study design, a comprehensive assessment of the applicability of these approaches to fQSM data is currently missing.

Here, we used ultra-high field 7T-MRI and fine-grained tonotopic mapping to characterize “unexpected” fQSM responses (i.e., those voxels with equal activation sign in fQSM and fMRI) and to assess the ability of this technique to discriminate between brain responses elicited by different perceptual features, specifically tone frequency. To do this, we used three approaches typically adopted in modern neuroimaging studies: the classic mass-univariate GLM, the population Receptive Field (pRF) method (Dumoulin and Wandell, 2008), and the Representational Similarity Analysis (RSA) (Kriegeskorte et al., 2008).

2. Methods

2.1. Subjects

Twelve healthy volunteers (6 females, aged 27 - 44 years, 33 ± 6 years old) with normal hearing and no history of neurological diseases or psychiatric disorders were recruited to participate in the study and underwent a 7 Tesla MRI scan session. All subjects received a medical interview, including a brain structural MRI scan, to exclude any disorder that could affect brain structure or function. All participants gave their written informed consent after the study procedures and potential risks had been explained. The study protocol was approved by the local Institutional Review Board (IRB) (Comitato Etico Area Vasta Nord Ovest - CEAVNO; Protocol No. 1485/2017) and the research was conducted in accordance with national legislation and the Declaration of Helsinki.

2.2. Experiment and stimulus design

Stimuli for tonotopic mapping consisted of trains of pure tones (rate: 10 tones per second; duration: 75 ms with 5 ms cosine ramp in loudness) selected from ten perceptually uniform frequency bands based on the Bark scale (Zwicker, 1961): (1) 100–200 Hz; (2) 300–400 Hz; (3) 510–630 Hz; (4) 770–920 Hz; (5) 1080–1270 Hz; (6) 1480–1720 Hz; (7) 2000–2320 Hz; (8) 2700–3150 Hz; (9) 3700–4400 Hz; (10) 5300–6400 Hz). We adopted this particular stimulation paradigm based on narrowband stimuli as it provides high sensitivity in detecting differences in frequency tuning (Langers et al., 2014). Pure tones were presented binaurally in blocks of 7.5 s followed by randomly selected rest periods of either 7.5 or 10 s. The loudness of each block was modulated by a cosine ramp of 0.3 s, to fade in and out and mitigate the startle caused by stimulus onset. The onset of the first stimulus block was preceded by a rest period of 20 s (including 10 s of dummy scans) and each fMRI run ended with an additional 5 s period of silence. A scheme of the stimulation paradigm for one fMRI run is presented in Supplementary Materials (Fig. S1). The ten frequency bands were played in a pseudorandom order across subjects and across the four runs that were acquired in the MRI session. Each frequency band was presented twice per run, summing up to a total of 20 trials per run and 80 trials per scan session, that is 8 trials per frequency band. The duration of one run was 5 min and 50 s, summing up to 23 min and 20 s for the whole functional scan. To ensure that all frequency bands were perceived as having comparable loudness, three subjects were asked to equalize the volume of 12 pure tones ranging 100–8000 Hz with respect to a 1000 Hz reference frequency. This procedure was performed during an EPI scan to account for the scanner noise. The equalization was performed via the QUEST adaptive psychometric method (Watson and Pelli, 1983), with an initial guess for the algorithm derived from the ISO-226 standard. Afterward, the loudness for each tone was derived via an interpolating fit and further adjusted for each subject to account for possible differences in scanner noise attenuation due to earphone positioning and head padding. Subjects were instructed to passively listen to the stimuli and keep their eyes closed during the entire acquisition.

Stimuli were designed in MATLAB 2017a (Mathworks, Natick, MA, USA) running Psychtoolbox and administered via MR-compatible in-ear earphones (VisuaStimDigital, Resonance Technologies, Los Angeles, USA), connected to a computer placed in the control room.

2.3. MRI system

Functional and anatomical MR images were acquired on a GE Healthcare Discovery MR950 7T MRI system (GE Healthcare, Chicago, Illinois) equipped with a two-channel transmitter/32-channel receiver head coil (Nova Medical, Wilmington, MA, USA) and a gradient system with maximum amplitude = 50 mT/m and slew rate = 200 mT/m/ms.

2.4. MRI acquisition

Functional scans were performed by using a 2D gradient echo EPI. Forty-nine slices were prescribed axially and acquired in interleaved ascending order (odd slices first). The prescription partially covered the brain starting from ventral regions, up to perisylvian frontal and parietal territories. The following acquisition parameters were employed for all functional runs: Echo Time (TE) = 21.3 ms, Repetition Time (TR) = 2.5 s, Flip Angle (FA) = 74°, Field Of View (FOV) = 230 × 230

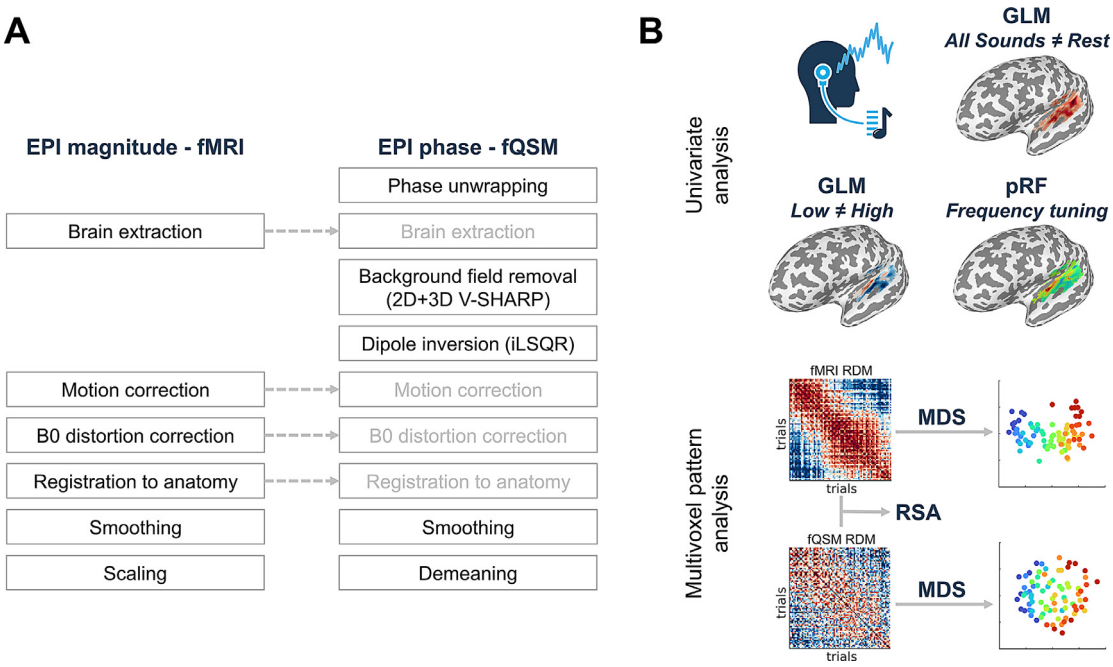

Fig. 1. Graphical summary of the reconstruction and preprocessing pipelines (panel A) and of the analysis that were performed on the fMRI and fQSM dataset (panel B).

mm^2, matrix size = 128 × 128, in-plane resolution = 1.8 mm, slice thickness = 1.8 mm, parallel imaging ASSET (Array coil Spatial Sensitivity Encoding Technique) acceleration factor = 3, fat suppression. No resampling was performed during image reconstruction to preserve native resolution.

Each subject underwent one fMRI session, consisting of four runs of tonotopic mapping. To correct for geometric distortions associated with phase-encoding direction, we set opposite gradient polarity (either anterior-to-posterior or posterior-to-anterior) for odd and even runs. Four "dummy" volumes were discarded at the beginning of each run to allow the magnetization to reach the steady-state. The number of acquired volumes for each tonotopy run was 136. For each functional scan, we acquired the complex-valued signal and reconstructed the magnitude and the phase images using a custom code running in MATLAB 2019a.

For anatomical reference, a T1-weighted image was acquired using an MP2RAGE sequence (Marques et al., 2010). This is a modified version of a Magnetization-Prepared Rapid Gradient Echo (MPRAGE) scan, based on the acquisition of two low-flip angle images at two different Inversion Times (TI). MP2RAGE sequence was prescribed axially to cover the whole brain and acquisition parameters were set as follows: TR = 6.6 ms; TE = 2.0 ms; Inversion Time $TI_{1,2}$ = 1000, 3200 ms; FA = 5°; voxel size = 0.8 × 0.8 × 0.8 mm^3, in-plane FOV = 220 × 220 mm^2; sagittal coverage = 176 mm; scan duration = 11′36″).

2.5. Functional QSM data reconstruction

A susceptibility map was computed for each acquired volume as follows. Firstly, the raw phase image of each volume was unwrapped via a Laplacian-based algorithm (Li et al., 2011; Schofield and Zhu, 2003). A brain mask was generated using the Brain Extraction Toolbox (*bet*) (Smith, 2002) in FSL 5.0.9 (FMRIB Software Library, Oxford centre for Functional MRI of the Brain, Oxford, UK) on the magnitude image and then used for the background phase removal. To this purpose, we employed an optimized pipeline for 2D EPI phase processing (Wei et al., 2016): the background phase was removed via a 2D version of the Laplacian-based method V-SHARP, followed by 3D V-SHARP (Schweser et al., 2011). This joint 2D and 3D approach solves the issue of phase inconsistencies across adjacent slices of 2D EPI. The 2D step removes the in-plane harmonic components of background noise and reduces the phase inconsistencies between slices; then, the 3D step removes the through-plane noise contributions. The iLSQR method (Li et al., 2015, 2011) was applied to tissue phase images of each time-point to obtain QSM maps. The algorithms used for phase processing and QSM reconstruction are implemented in STI Suite (MATLAB toolbox, available at https://people.eecs.berkeley.edu/~chunlei.liu/software.html from UC Berkeley, Berkeley, CA, USA). The reconstruction pipeline is illustrated in Fig. 1A.

2.6. Preprocessing of anatomical data

MP2RAGE raw data were reconstructed offline with a custom MATLAB code using Orchestra, a GE Healthcare reconstruction framework. Images corresponding to each inversion time were obtained via Autocalibrating Reconstruction for Cartesian imaging (ARC) followed by adaptive coil combination (Walsh et al., 2000) and vendor-provided gradient non-linearities correction. The final MP2RAGE image was obtained by combining the images acquired with different TIs (Marques et al., 2010) to produce T1-weighted anatomical images virtually free of intensity bias. After reconstruction, the anatomical images were rigidly aligned along the Anterior Commissure (AC) - Posterior Commissure (PC) plane (AC-PC). Specifically, an affine transformation (12 degrees of freedom) was computed to transform the T1-weighted image into MNI space using *flirt* (Jenkinson et al., 2012) in FSL 5.0.9. Then, the transformation was converted to rigid body transform (6 degrees of freedom) and applied to the anatomical dataset. Brain extraction was performed via antsBrainExtraction.sh routine in ANTs (Advanced Normalization Tools), using the OASIS dataset as a template. Tissue class segmentation was performed in SPM12 (Penny et al., 2011) to obtain gray and white matter probabilistic maps that were then resampled to EPI spatial resolution. Linear and non-linear registration to the MNI152 template were performed via *3dQwarp* in AFNI (Cox, 1996) adopting the wsinc5 interpolation method.

2.7. Preprocessing of functional data

Data were visually inspected to ensure the absence of excessive motion and scanning artifacts. Preprocessing of the functional datasets was performed in AFNI. Motion correction was carried out via *3dvolreg* in two sequential steps: in the first iteration, all volumes were aligned to the first of each time series to compute the framewise displacement between each pair of successive time points; then, the registration was repeated using the volume showing the smallest displacement as a reference. This procedure ensures that the reference time point is not corrupted by sudden head motion. Rigid body transformations (6 degrees of freedom) were computed and applied to functional time series. Head motion parameters were plot and inspected to verify data quality and the absence of a significant correlation between motion and stimulus timing. Non-brain tissues were removed using *bet* routine in FSL 5.0.9. B0 distortion was corrected by applying the following steps: the two pairs of scans acquired with the same gradient polarity were aligned together and averaged. Afterward, the two average images with opposite polarity were coregistered using 3dQwarp and the "meet in the middle" algorithm (*-plusminus* option). After computing the affine transformation matrix of the undistorted average EPI image to the skull-stripped T1-weighted scan via *align_epi_anat.py* routine, the two transformations (the B0 distortion correction and the alignment to the anatomical scan) were concatenated and applied simultaneously to the functional scans via *3dNwarpApply*. Data were spatially blurred to a Full-Width at Half-Maximum (FWHM) of 6 mm using *3dBlurToFWHM*, a routine that iteratively estimates and increases the smoothness of data until reaching the desired level. Lastly, the time series were demeaned and scaled to percent signal change.

Functional QSM data were motion-corrected and aligned to the anatomical image by applying the transformation computed for conventional fMRI data. To preserve fQSM quantitative information, we applied nearest-neighbor interpolation method, in both fQSM and fMRI pipelines for consistency. Then, data were smoothed up to 6 mm FWHM (*3dBlurToFWHM*) and demeaned. Scaling was avoided to preserve the quantitative information of the variation of tissue susceptibility, here reported in parts per billion (ppb). The preprocessing steps are summarized in Fig. 1A.

2.8. Selection of tone-responsive areas

For each subject, we used AFNI's *3dDeconvolve* to perform a mass-univariate voxelwise GLM analysis (Friston et al., 1994) on fMRI and fQSM data. Regressors for each individual trial were created by convolving a boxcar function with the canonical hemodynamic response function. Polynomial drifts and six motion parameters (three translations and three rotations) were included as nuisance regressors. For conventional BOLD fMRI, voxels responding to auditory stimulation - i.e., *All Sounds* > *Rest* - were identified by performing a non-parametric permutation test (two-tailed) on the t-statistic map of each trial using FSL *randomize*, setting a threshold of $p < 0.05$ voxel-wise corrected. We selected the two largest clusters with positive fMRI response for each subject, together with voxels showing significant negative responses, so as to obtain a functionally defined mask of the Sound Responsive Area (SRA). Even though negative fMRI activations are not usually taken into account, their inclusion in the current analysis allows us to have a fair comparison between conventional BOLD fMRI and fQSM, where the presence of both positive and negative activations is frequently acknowledged. Similarly, a region of active voxels in fQSM with both positive and negative responses was defined via a permutation test with the same statistical threshold used for conventional fMRI. After alignment to the MNI space, a probabilistic SRA Region Of Interest (ROI) was computed by summing the masks across subjects. The peak values of R^2 obtained in SRA for fMRI and fQSM for all subjects were compared with a paired *t*-test.

2.9. Tonotopic mapping

A first contrast of interest was computed on single-subject GLM coefficients, testing the "Low frequencies" (pure tones ranging from 100 to 630 Hz; frequency bands 1 to 3) > "High frequencies" (pure tones ranging from 2700 to 6400 Hz; frequency bands 8 to 10) contrast. In addition, to estimate the frequency tuning curve of voxels in the SRA ROI, we employed the population Receptive Field (pRF) approach (Dumoulin and Wandell, 2008). The population response was modeled as a one-dimensional Gaussian function, defined over log-scaled frequency (Thomas et al., 2015). The center frequency f_0 spanned the whole range of frequencies played during stimulation, from 100 Hz to 6400 Hz, covering an interval of 6 octaves, with a step size of 0.25 octaves. The values of the standard deviation σ ranged from 0.25 to 4 octaves, with 0.25 octaves step size. The expected response for a population whose tuning is described by one of the Gaussian functions is computed by evaluating the Gaussian curve at the frequency played at each time point. Models were fitted to the data via linear regression, after cleaning out the contribution of nuisance variables (i.e., drifts and head motion), and the tuning for each voxel was determined by selecting the combination of f_0 and σ that maximizes the t-score of the fit, that is β/SE where β is the coefficient of the linear regression and SE is the standard error of the fit. For fQSM data, we selected the Gaussian function that provided the maximum negative t-score, as one should expect the fQSM activation to be sign-flipped as compared to conventional fMRI. The similarity of pRF maps obtained from fMRI and fQSM for each subject was quantified using Pearson's correlation. Statistical significance of the correlation coefficient was evaluated via permutation testing.

2.10. Multivariate pattern analysis

To evaluate the response pattern of SRA and to assess the ability of this region in discriminating pure tones based on their frequency, we employed RSA (Kriegeskorte et al., 2008). We conducted this analysis in an ROI defined as the intersection between fMRI and fQSM SRA masks, which identifies task-selective voxels regardless of the technique. For both fMRI and fQSM and for each subject, we obtained Representational Dissimilarity Matrices (RDM) by computing the pairwise correlation distance between tone-specific activity patterns. The correspondence between the fMRI and fQSM RDMs was tested through Pearson's correlation coefficient and statistical significance was assessed via permutation testing. Specifically, in each iteration, stimulus labels of fQSM trials were shuffled thus to obtain a null RDM, which was correlated with the one coming from conventional fMRI. This procedure generated a null distribution (10^5 permutations), which was used to test the significance of the actual correlation value. Lastly, to visualize the functional mapping of pure tones in the SRA region obtained from fMRI and fQSM data, we performed Multidimensional Scaling (MDS; *mdscale* function in MATLAB). Both single-subject and group-average RDMs were visualized in a two-dimensional MDS space. Analyses performed in this study are summarized in Fig. 1B.

3. Results

3.1. Data quality and phase artifacts

All subjects involved in the study completed the exam session. However, two of them (M-28yo, F-27yo) reported having fallen asleep during the scan. Moreover, the analysis of motion parameters revealed extreme head motion for another subject (M-32yo): nearly 30% of total timepoints (up to 78% in one of the four runs) were corrupted by excessive framewise displacement (> 0.3 mm). These three subjects were not included in further analyses.

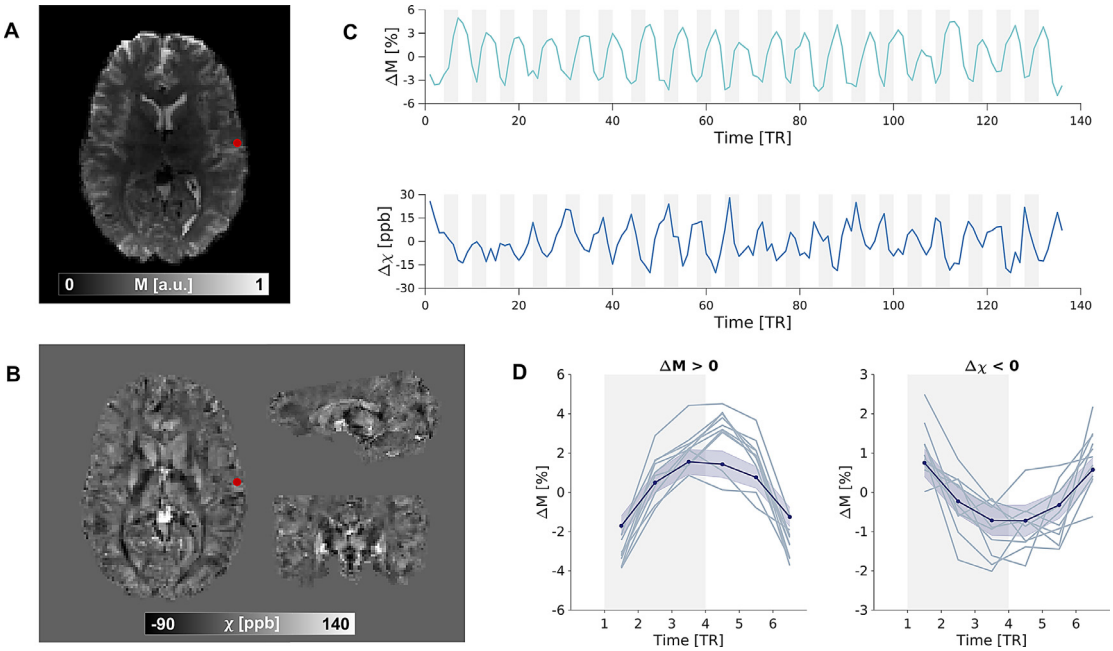

Fig. 2. In panel A, an exemplary T2*-weighted image obtained with EPI is presented, while panel B shows the corresponding QSM image obtained from the phase of the same acquisition. The optimized joint 2D-3D background field removal enables the reconstruction of susceptibility maps from 2D EPI with no phase inconsistencies across slices. Panel C shows the time course during one run of one exemplary voxel in SRA, indicated by the red dot in panel A and B, for fMRI (top) and fQSM (bottom) signal. The gray shaded area indicates stimulus presentation. In panel D we reported the average peristimulus plot for a voxel with positive fMRI and negative fQSM response (blue line, the shaded area indicates the standard error). The gray lines represent the peristimulus plot for an individual trial of each band for a representative subject. The gray shaded area indicates the stimulus period, lasting 3 TRs, that is 7.5 s (For interpretation of the references to color in this figure legend, the reader is referred to the web version of this article.).

An exemplary fQSM image obtained from the 2D-EPI acquisition by applying the optimized background phase removal workflow (Wei et al., 2016) is shown in Fig. 2B, together with the corresponding T2*-weighted image (Fig. 2A). The across-slices phase-inconsistency artifact also reported in previous fQSM studies (Balla et al., 2014; Özbay et al., 2016) was removed. Fig. 2C shows fMRI and fQSM activity of a voxel located in the auditory cortex for a single functional run. Instead, Fig. 2D depicts the peristimulus plots computed in a voxel showing positive fMRI and negative fQSM responses.

3.2. GLM analysis and tone-responsive areas

Results of the *All Sounds > Rest* contrast showed that the average R^2 peak across subjects in SRA was 0.7 ± 0.1 for fMRI and 0.4 ± 0.1 for fQSM (systematically lower in fQSM than fMRI; $p < 10^{-6}$ in a paired *t*-test). Also, R^2 maps obtained from fMRI and fQSM data were significantly correlated (Pearson's correlation coefficient was 0.434, $p < 0.001$; Fig. 3A). A linear fit yielded an angular coefficient of 0.17 ($R^2 = 0.19$), indicating that the variance of fMRI data explained by the model is higher than for fQSM data (Fig. 3A). Further, the average maximum signal increment observed for magnitude EPI during the task was 9 ± 1%. For fQSM, the maximum decrease in susceptibility was -47 ± 14 ppb, ranging from −79 ppb to −35 ppb depending on the subject. Maximum positive fQSM response was 39 ± 14 ppb. At the statistical significance threshold chosen in the current study, the minimum detectable variation of susceptibility ranged from −0.006 ppb to −0.9 ppb depending on the subject, with a median of −0.023 ppb.

The contrast All Sounds > Rest is shown in Fig. 4 for fMRI and fQSM on the reconstructed cortical surface of each subject.

The probabilistic SRA ROI projected onto a group level MNI cortical mesh is shown in Fig. 5. The tone-responsive areas identified by the two techniques differed in size, with the fQSM ROI being approximately 15 ± 9% of the SRA ROI defined by fMRI. Also, the definition of SRA using fQSM data had higher inter-subject variability. Moreover, differently from fMRI results, voxels in these regions showed both increments and decrements in susceptibility (Fig. 3B). For voxels with responses of opposite sign in fMRI and fQSM, we reported significant Pearson's correlation $r_- = -0.495$ ($p < 0.001$) between t-stats values, while $r_+ = 0.212$ ($p < 0.001$) was found for voxels with responses with the same sign. The fraction of voxels yielding a positive fQSM response was 27 ± 10% in the SRA ROI defined by fQSM. This ratio dropped to 14 ± 10% when we considered "unexpected" voxels in the overlap between the tone-responsive areas of fMRI and fQSM (Fig. 3C).

Voxels belonging to White Matter (WM) and Gray Matter (GM) were studied separately according to the segmentation of the anatomical image with a probability threshold of 0.5. The fraction of active voxels belonging to gray matter structures was 65 ± 4% for fMRI and 73 ± 8% for fQSM (Fig. 6A). This statistically significant difference ($p < 0.01$ in a Wilcoxon signed rank test) indicates that fQSM provides patterns of activation that are more spatially specific than the one obtained via fMRI. We reported that the fraction of voxels with fQSM response of opposite sign with respect to fMRI was higher in GM than in WM. In fact, while in GM the fraction of voxels with "unexpected" fQSM response was 12%, in WM it was 42% (Fig. 6B). The anatomical localization of active voxels can be also indicated by their structural tissue susceptibility, as measured by the fQSM time average. Fig. 6C shows the relationship between the average susceptibility of tone-responsive voxels and the sign and magnitude of its response. Negative fQSM responses generally yielded a higher R^2 value with respect to positive fQSM. The median of the tissue susceptibility distribution in an fQSM t-stat interval shifts towards negative values when fQSM response becomes positive (Fig. 6D). As negative values in QSM indicate the presence of a diamagnetic source, such as myelin, they are typically found in WM structures, whereas positive χ values in GM. Thus, fQSM activation of the same sign as fMRI were mostly located in WM, while in GM the expectations on fQSM behavior were met in the great majority of voxels.

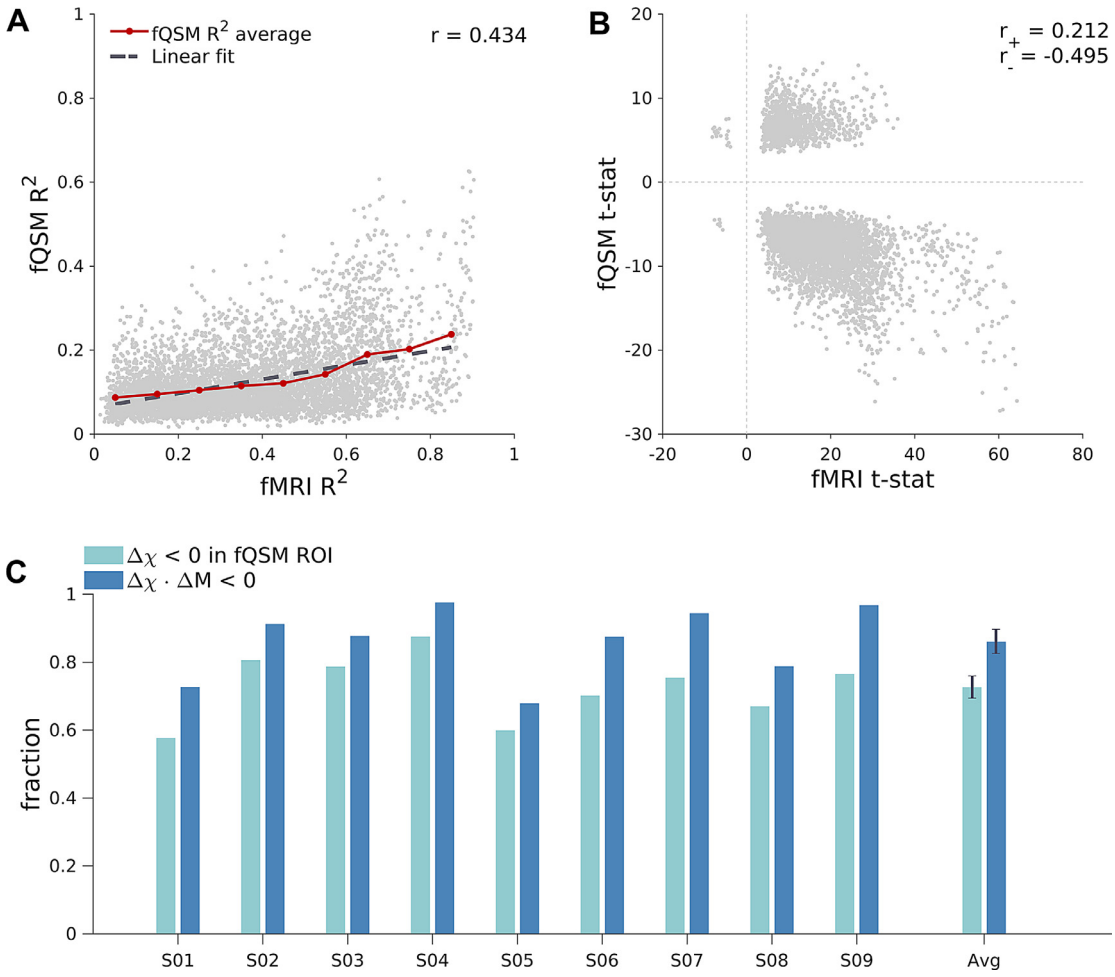

Fig. 3. Scatter plot showing the relationship between fMRI and fQSM R^2 values (panel A) of voxels that are identified as tone-responsive ($p < 0.05$ voxelwise corrected) by both techniques, for all subjects. The red line indicates the average fQSM R^2 over 0.1-wide fMRI R^2 intervals and the result of the linear fit is displayed as a gray dashed line. We reported Pearson's correlation coefficient $r = 0.434$ ($p < 0.001$) and an angular coefficient of 0.17 from the linear fit ($R^2 = 0.19$). In panel B, the scatter plot shows the fQSM t-stat values corresponding to fMRI t-stat values. For voxels with responses of opposite sign we reported Pearson's correlation coefficient $r_- = -0.495$ ($p < 0.001$), while $r_+ = 0.212$ ($p < 0.001$) was found for voxels with responses with the same sign. Panel C displays the fraction of voxels showing negative fQSM response in the SRA ROI defined by fQSM (light blue) and voxels showing opposite response with respect to fMRI in shared tone-responsive areas (dark blue). The error bars indicate the standard error of the mean (For interpretation of the references to color in this figure legend, the reader is referred to the web version of this article.).

3.3. Comparison of tonotopic mapping

Regions in SRA that responded preferentially to lower and higher frequencies according to GLM analyses are displayed in the first two columns of Fig. 7. In fMRI data, 34 ± 16% of voxels were selective for higher frequencies, whereas in fQSM this fraction was significantly higher ($p < 0.05$ in a paired t-test), reaching 52 ± 3% and yielding more balanced GLM contrast maps. We obtained the fine-grained mapping of the frequency tuning of SRA voxels for both fMRI and fQSM data (third and fourth columns in Fig. 7, respectively). Even though the maps obtained from fMRI data were smoother, fQSM frequency tuning maps showed the expected rostro-caudal high-low-high organization. Also, this arrangement extended to areas that did not reach significance for fQSM at the threshold selected in this study. The similarity between results obtained via fMRI and fQSM was also testified by the significant correlation between the pRF patterns ($p < 0.001$ for each individual; across-subjects average $r = 0.22 \pm 0.11$).

3.4. Similarity of activation patterns

The group average RDMs obtained from both fMRI and fQSM data are shown in Fig. 8A. Single-subject RDMs are reported in Supplementary Materials (Fig. S2). RSA analysis revealed significant correspondence between the RDMs obtained from the two approaches ($r = 0.72$ for the group average, 0.49 ± 0.15 for individual subjects, $p < 10^{-5}$).

The results of the MDS analysis are shown for the group-average RDMs and for two representative subjects in Fig. 8B. The scatter plots for each individual subject are reported in Fig. S3 in Supplementary Materials. The MDS analysis on the group-average RDMs, as well as the results on the single subject, showed that trials of the same stimulus condition were clustered together along the first dimension for both fMRI and fQSM. As shown in Fig. S4 in Supplementary Materials, the second dimension highlighted two clearly distinguished clusters corresponding to the trials belonging to EPI runs with opposite polarities. Despite being noisier than fMRI, the activation patterns in fQSM retained enough information to enable the mapping of a fine-grained, topographically-arranged organization of SRA.

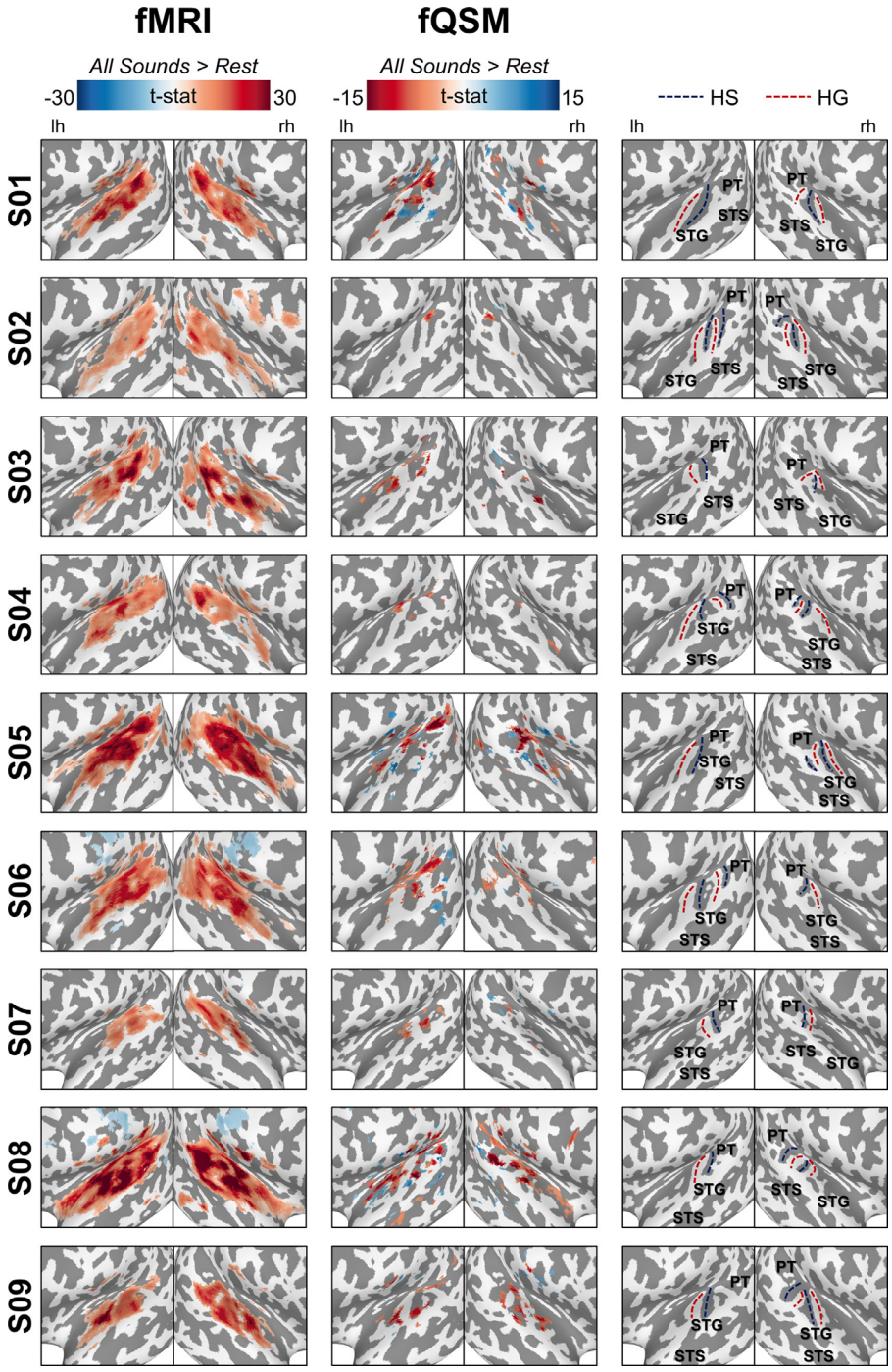

Fig. 4. Activation maps overlaid onto the inflated cortical surface mesh of each subject. The first two columns display the t-statistics obtained for each subject by summing the response to all stimulus trials in the SRA ROI identified via non-parametric permutation test ($p < 0.05$ voxelwise corrected), for fMRI and fQSM respectively. The colormaps corresponding to fMRI and fQSM are inverted to take the sign inversion of the response into account and allow a more direct comparison. The third column reports the anatomical landmarks of interest: Superior Temporal Sulcus (STS), Superior Temporal Gyrus (STG), Planum Temporale (PT) and Heschl's Sulcus (HS, blue line) and Gyrus (HG, red line) (For interpretation of the references to color in this figure legend, the reader is referred to the web version of this article.).

4. Discussion

In the current study, we acquired a complex-valued 2D-EPI dataset in a sample of healthy subjects using a 7T MRI scanner to assess the usefulness of fQSM in up-to-date human neuroimaging research. We particularly focused on the evaluation of fQSM spatial specificity and on the characterization of its sensitivity in discriminating patterns of activation associated with different stimulus conditions.

We report that, in fQSM data, voxels significantly activated by listening to pure tones are less numerous, but also more likely located in the gray matter, than above-threshold voxels identified using canonical fMRI. This suggests that the lower sensitivity of fQSM is, indeed, paralleled by higher spatial specificity. Interestingly, "unexpected" positive fQSM activations are mainly limited to white matter. Moreover, both univariate GLM and pRF analyses provide similar results when comparing the two acquisition methods. Nevertheless, while maps obtained

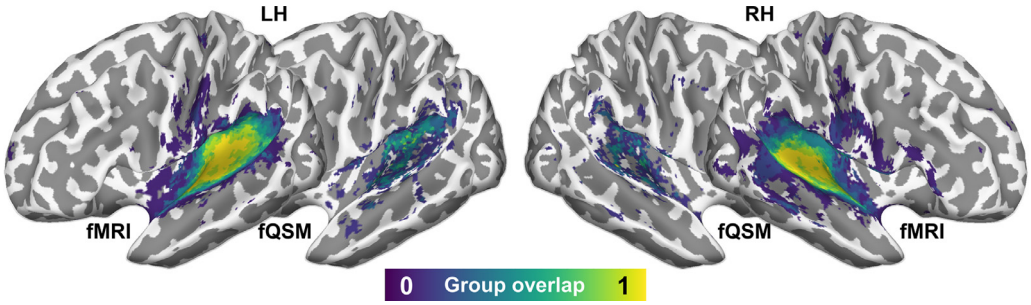

Fig. 5. Probabilistic SRA ROIs obtained by computing the overlap in the MNI space of the SRAmasks of all subjects. The ROI computed via fQSM was smaller and showed less inter-subject overlap than the fMRI ROI.

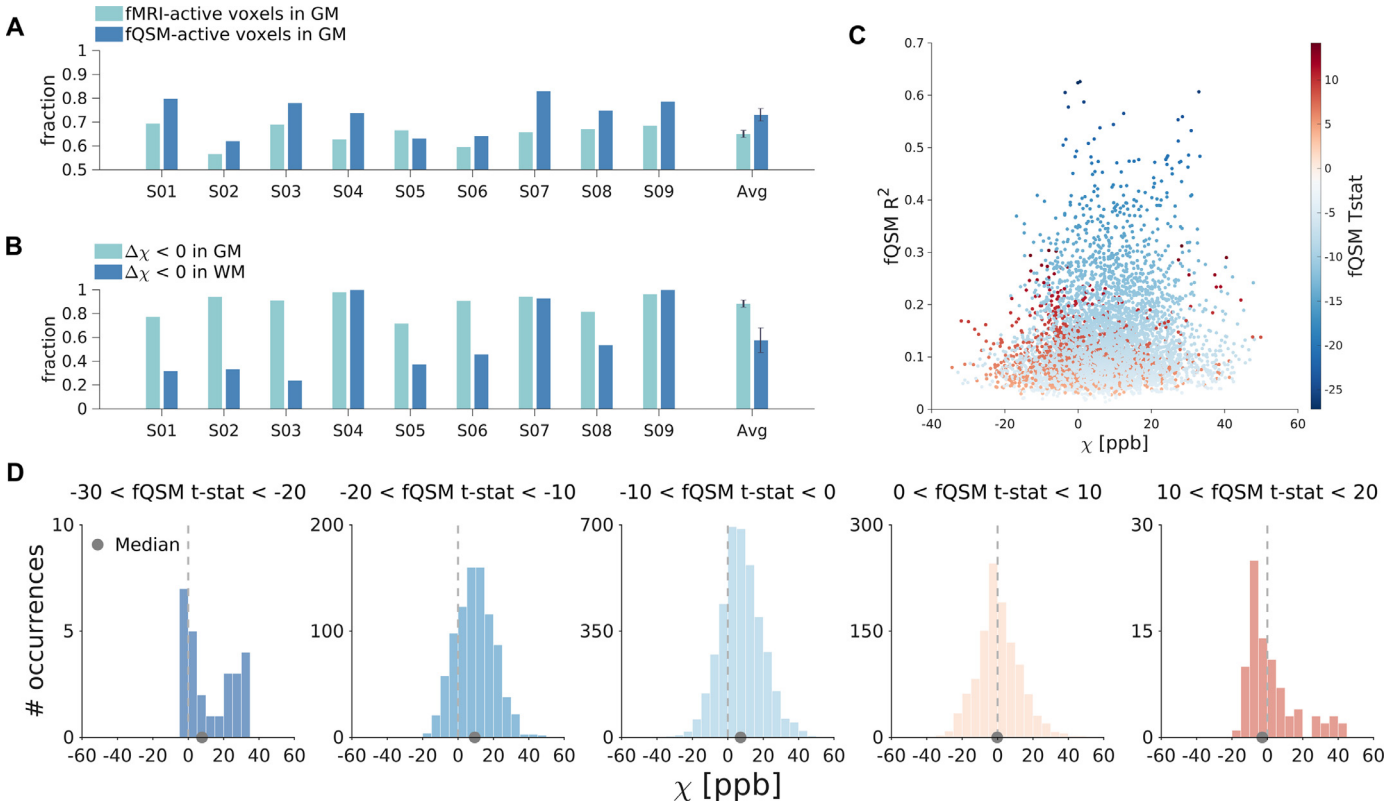

Fig. 6. Anatomical distribution of active voxels. The fraction of voxels that belong to gray matter structures and show a significant response at the statistical threshold selected in this study was higher in fQSM (dark blue) than in fMRI (light blue) (Panel A), indicating that fQSM yields higher spatial selectivity than fMRI. The error bars indicate the standard error of the mean. Panel B shows the fraction of voxels with negative fQSM response in gray matter (light blue) and white matter (dark blue) for each subject and averaged over the whole group, highlighting that voxels with positive fQSM response were mostly found in white matter. Panel C displays in a scatter plot the relationship between fQSM R^2 values and the structural tissue susceptibility χ for all subjects. The colors of the dots represent the magnitude of fQSM response. Panel D shows the data plotted in panel C after dividing the values of the t-statistics into five intervals. The colors of the histogram bars represent the intensity of the fQSM response, while the gray dot indicates the median of the distribution. It can be seen that the median susceptibility shifts towards negative values when the response becomes positive. This suggests that the voxels showing positive responses were mainly located in white matter (For interpretation of the references to color in this figure legend, the reader is referred to the web version of this article.).

from fMRI are smoother in their spatial distribution, those coming from fQSM show a patchier organization and voxel tunings are more equally represented across the whole frequency range. This evidence is - again - in favor of the higher specificity of fQSM in capturing fine spatial variations related to the functional architecture of tone selective brain areas. Lastly, the representational similarity analysis highlights a significant correlation between patterns of brain activity derived from fQSM and canonical fMRI data.

In light of all this, our findings indicate that when univariate and multivariate methods are applied to fQSM data, they provide biologically plausible results and that fQSM and canonical fMRI data complement each other in the study of brain activity.

In agreement with previous studies (Balla et al., 2014; Bianciardi et al., 2014; Chen et al., 2013; Costagli et al., 2019; Özbay et al., 2016; Shih et al., 2021; Sun et al., 2016), when the same statistical threshold is applied, the extent of tone-responsive areas identified by fQSM is five- to ten-fold smaller as compared to the one identified by fMRI. However, fQSM is sufficiently sensitive to detect significant variation of susceptibility in the order of −0.01 ppb, that is two orders of magnitude lower than what expected for pial veins (Balla et al., 2014). This suggests its capability of revealing not only strong sources of susceptibility variation, such as big vessels that yield a signal alteration in the order of −10 ppb, but also weak activations in the parenchyma. Also, fQSM activation maps have a significantly

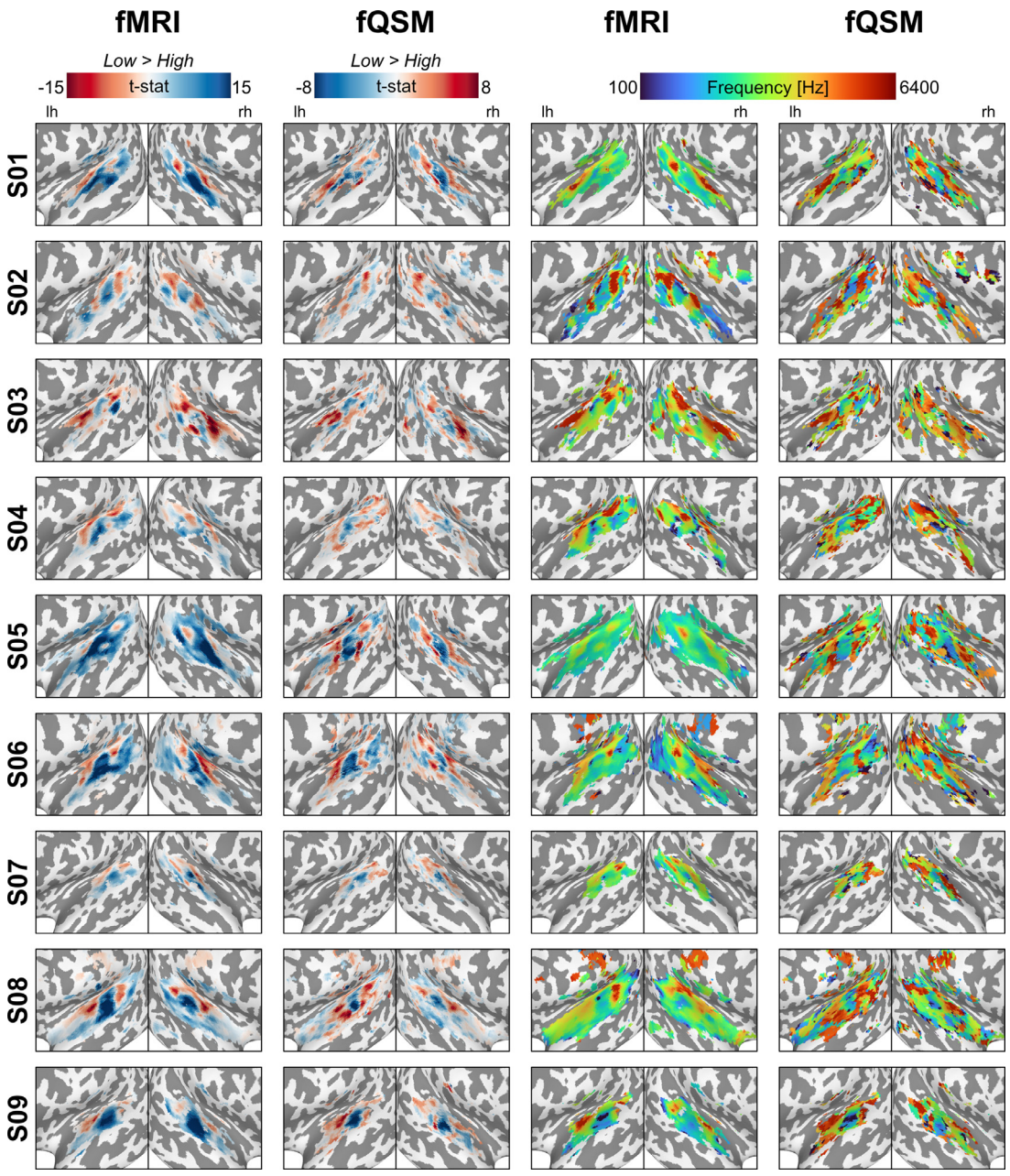

Fig. 7. GLM-contrast and pRF maps. The first two columns display the areas in SRA ROI that responded preferentially to low frequencies belonging to the first three frequency bands (100–630 Hz) with respect to the high frequencies from the last three bands (2700–6400 Hz), for fMRI and fQSM respectively. The colormaps corresponding to fMRI and fQSM are inverted to take the sign inversion of the response into account and allow a more direct comparison, so that low and high frequencies are consistently represented in blue and red respectively. The third and fourth columns show the results of the pRF approach for each subject for fMRI and fQSM respectively. The maps obtained by fMRI were smoother but a comparable pattern of frequency tuning preference was retrieved also for fQSM (For interpretation of the references to color in this figure legend, the reader is referred to the web version of this article.).

greater fraction of voxels lying in gray matter tissues than fMRI, which we interpreted as a clue of higher spatial specificity. This is built on the assumption that brain activity should be typically observed in gray matter rather than white matter. By testing the spatial distribution of active voxels at different statistical thresholds, we reported higher specificity of fQSM for activations in gray matter for the majority of subjects, as described in Supplementary Materials and Supplementary Fig. S5. However, a conclusive proof of this statement would require a ground truth measurement for tonotopic mapping. The higher spatial specificity of fQSM can be explained by the deconvolution of the dipole kernel performed during QSM reconstruction and the subsequent removal of the non-local effect. Indeed, in conventional fMRI the perturbation of the magnitude signal extends to voxels surrounding the foci of the neural activation, hindering the accurate mapping of the true activation site (Schenck, 1996). Notably, the increased spatial specificity is not canceled by the small amount of spatial smoothing that was applied to the data, suggesting that the non-local dipole effect acts on a larger-scale distance. On the other hand, spatial smoothing allowed direct comparison with fMRI data and increased statistical robustness (Worsley and Friston, 1995). In addition, the analysis repeated with no spatial blurring applied yielded analogous results, indicating that activation pattern can be retrieved by fQSM data even in the absence of smoothing, as shown in Supplementary Fig. S6.

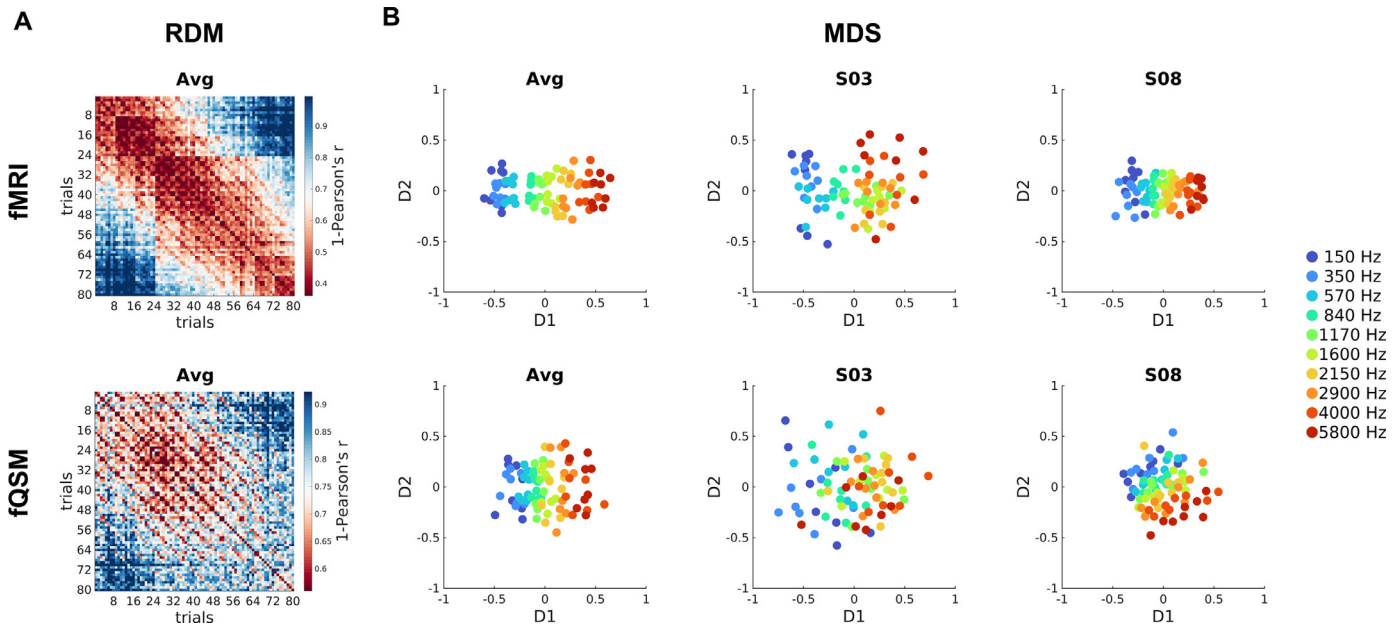

Fig. 8. RDMs and the results of MDS analysis. Panel A shows the group average RDMs computed via the correlation distance between activation patterns in SRA ROI for fMRI (top) and fQSM (bottom). In panel B, the scatter plots representing in a 2-dimensional MDS space the group-average RDMs and the RDMs of two representative subjects are displayed. The first row refers to fMRI results while the second corresponds to fQSM. The colors represent the central frequency of the band of each trial. The activation patterns of trials corresponding to the same stimulus condition clustered along the first MDS dimension.

Despite negative fQSM responses are expected to colocalize with positive fMRI activation, previous studies (Balla et al., 2014; Chen et al., 2013; Costagli et al., 2019; Özbay et al., 2016) reported sign inversion of the fQSM activity, that is voxels whose susceptibility time series showed significant positive correlation with stimulus presentation, just as the corresponding fMRI time series. This was especially observed in regions close to strong susceptibility sources such as large veins (Özbay et al., 2016), suggesting that in these areas the QSM reconstruction step failed in completely removing the non-local field components (Balla et al., 2014; Özbay et al., 2016). On the other hand, positive fQSM was reported for several reconstruction methods, analysis approaches and acquisition parameters, indicating that it may underlie some physiological information. In this work, we observed the same effect and attempted to characterize its biophysical properties. Specifically, we characterized the anatomical substrate underlying these observations by labeling each activated voxel as belonging to gray or white matter, so as to test whether "unexpected" fQSM activations depended on the underlying anatomical structure. The labeling operation was performed based both on the tissue class segmentation obtained from the T1-weighted anatomical image and on the time-average susceptibility value of each voxel. We reported that the voxels showing positive fQSM activation were mainly located in white matter, while in gray matter more than 90% of voxels display the expected behavior. In fact, in our data, GLM contrasts were minimally affected by unexpected fQSM responses. Instead, the interpretation of activations in white matter is not trivial, even for conventional fMRI, and represents an open question in neuroscience (Gawryluk et al., 2014). It is acknowledged that the conventional fMRI models may not be suitable to detect white matter task-specific activations (Li et al., 2019) and that the lower density of vessels reported in white matter reduces the contribution of cerebral blood flow and volume to the fMRI signal (Gawryluk et al., 2014). Moreover, the anisotropic vascular architecture in white matter affects the GRE signal, i.e., the apparent $R2^*$ and magnetic susceptibility, as well as cerebral blood flow and volume, whose measured values depend on the orientation of vessels with respect to the static magnetic field B_0 (Hernández-Torres et al., 2017). Hence, the mismatch between fMRI and fQSM and its prevalence in white matter may be related to artifacts or it may be due to the detection of different contributions to the signal which could be interpreted by developing improved biophysical modeling, as the well-established model adopted for the cerebral cortex might be inadequate. Even though our characterization suggests that morphological properties of brain tissues are implicated in the generation of positive fQSM responses, further investigations are needed to clarify its underlying mechanisms.

On these premises, we compared fQSM and fMRI responses to different stimulus conditions, that is to different sound frequencies, using both univariate and multivariate methods. The "Low > High frequency" GLM map revealed the expected rostro-caudal high-low-high functional organization in SRA (Brewer and Barton, 2016; Da Costa et al., 2015, 2011; Dick et al., 2012; Humphries et al., 2010; Saenz and Langers, 2014; Thomas et al., 2015). The morphological, functional and topographical organization of the human auditory cortex is highly variable (Moerel et al., 2013; Ren et al., 2021; Saenz and Langers, 2014; Thomas et al., 2015) and both fMRI and fQSM maps displayed high inter-subject and inter-hemispheric variability. Voxels selective for higher frequencies were significantly more represented in fQSM-based maps than in the corresponding fMRI data, leading to more balanced GLM contrast maps. Accordingly, the pRF method yielded fine-grained frequency-tuning maps that were similar for fQSM and fMRI, as testified by Pearson's correlation coefficient. The smoother appearance of fMRI tonotopic maps may relate to the intrinsic blurring of the magnitude signal due to dipole effect, or to the higher noise level in fQSM. A test-retest analysis performed by splitting the data into two halves proved the reproducibility of fQSM responses. In addition, the stability of the pRF estimates of frequency tuning was demonstrated by performing the fitting operation on a partition of the data and testing its reliability on the remaining part. Test-retest reproducibility was lower in fQSM with respect to fMRI and stable fQSM response was reported in a smaller fraction of voxels, likely due to the different sensitivity and specificity of the two techniques. Nonetheless, the high-low-high frequency tuning pattern was successfully retrieved. These analyses are described in the Supplementary Materials and shown in Supplementary Figs. S7 and S8.

Multivoxel pattern analysis confirmed the correspondence between fMRI and fQSM information. For each technique, we obtained RDMs from patterns of activation corresponding to each stimulus trial and at-

tested their similarity via RSA. Non-metric multidimensional scaling was employed to reduce matrix dimensionality and unveil RDMs structure. In both cases, the trials clustered along the first MDS dimension based on their frequency. Hence, similarly to fMRI, fQSM captures variations in brain activity associated with the processing of perceptual features. Unexpectedly, despite the correction for susceptibility-induced geometric distortions, the second dimension distinguished between trials belonging to acquisition runs with opposite phase-encoding polarities, which then left a trace in the response pattern of both techniques.

One interesting application that fQSM might find in neuroscience research concerns the study of cortical columnar- or layer-specific activation via sub-millimetric fMRI acquisitions, as the spatial accuracy of activity localization would be a powerful tool in disclosing small-scale functional differentiation and architecture. However, in order to enable such application, future studies should test whether fQSM sensitivity is sufficient to detect brain activity using sub-millimetric spatial resolution and no spatial smoothing. In this case, one limitation would be represented by the small brain coverage, which would disrupt fQSM quantification accuracy. In fact, QSM values are affected by partial coverage of the brain, especially in slices near the boundaries (Elkady et al., 2016; Karsa et al., 2018), even though deep learning approaches may mitigate this issue (Zhu et al., 2021). In this study, we did not reach whole-brain coverage but the cortical areas of interest (i.e., SRA) are far from the borders of the acquired volume. Other factors affecting susceptibility quantification concern the choice of voxel size (Karsa et al., 2018; Zhou et al., 2017), echo time (Biondetti et al., 2020; Cronin et al., 2017; Lancione et al., 2019; Sood et al., 2017), and the orientation of the subject's head with respect to the external magnetic field, due to the tensorial nature of magnetic susceptibility (Li et al., 2012). However, this does not represent a confounding factor in gray matter, as susceptibility anisotropy in the brain is mainly related to the highly ordered microstructure of myelin sheath (Lancione et al., 2017; Li et al., 2012; Liu et al., 2011; Wharton and Bowtell, 2015). Further studies are needed to assess the accuracy of quantification of dynamic variations in tissue oxygenation obtained from fQSM.

In the current study, the use of an optimized pipeline for the processing of the phase of 2D-EPI data enabled the reconstruction of susceptibility maps devoid of phase inconsistency artifacts, reported in previous works (Balla et al., 2014; Özbay et al., 2016). The following functional processing pipeline was derived from the canonical workflow for fMRI with some minor adjustments: spatial transformations were computed on the magnitude images and then applied to susceptibility maps and sign inversion of fQSM time series with respect to fMRI signal was taken into account when computing statistics and when fitting pRF models.

One limitation of this study is related to the lack of a ground truth for non-invasive *in vivo* brain functional mapping, as magnitude-based fMRI only represents a surrogate of neural activation with well-known limits concerning spatial specificity. As for the studies on the neurophysiological correlates of BOLD activations (Logothetis et al., 2001), simultaneous recording of fQSM data and local field potentials or multi-unit spiking activity are needed to address this issue. Also, activations obtained from fQSM and spin-echo (SE) fMRI should be compared, as SE-EPI are characterized by higher spatial accuracy (Yacoub et al., 2007).

While the relatively small sample size included in the current study could be considered a limitation, the results were obtained at single-subject level. Moreover, the high across-participants consistency of results for a wide range of analyses further corroborates the reliability of findings.

In conclusion, fQSM produces activation maps that are complementary to those obtained from conventional fMRI, as they seem to be characterized by a higher spatial specificity, though further studies comparing fQSM activation maps to ground truth measurement are needed. Not only have we been able to produce fine-grained tonotopic maps using univariate methods, but we also demonstrated that multivariate techniques can be applied to fQSM activity to access brain regional information content. Importantly, because fQSM is quantitative, information obtained at different scanning sites may be compared, thus providing a valuable, novel and cost-effective tool for pooling together data from different studies, including longitudinal as well as consortium and multicentric research and clinical projects. Of note, our results indicate that positive fQSM responses do not affect the interpretation of activations or contrasts of interest. Lastly, thanks to its higher spatial specificity, fQSM can detect brain activity more precisely, providing finer functional cerebral maps for brain surgery planning, as well as for other clinical investigations.

Data and code availability statement

Data and code may be provided to interested researchers upon request to the corresponding author, after clearance from the IRB.

Declaration of Competing Interest

The authors declare no conflict of interest.

Credit authorship contribution statement

Marta Lancione: Conceptualization, Methodology, Software, Formal analysis, Investigation, Visualization, Writing – original draft. **Mauro Costagli:** Conceptualization, Methodology, Software, Investigation, Funding acquisition, Writing – original draft. **Giacomo Handjaras:** Conceptualization, Methodology, Software, Formal analysis, Visualization, Writing – original draft. **Michela Tosetti:** Conceptualization, Resources, Funding acquisition, Project administration, Writing – review & editing. **Emiliano Ricciardi:** Conceptualization, Project administration, Writing – review & editing. **Pietro Pietrini:** Conceptualization, Funding acquisition, Writing – review & editing. **Luca Cecchetti:** Conceptualization, Methodology, Software, Formal analysis, Visualization, Supervision, Writing – original draft.

Acknowledgments

This study was supported by a PRIN grant (201755TKFE) to Pietro Pietrini by Italian Ministry of Education University and Research. This study was also partially supported by grants "RC 2018–2020" to IRCCS Fondazione Stella Maris, funded by the Italian Ministry of Health. The authors would like to thank Dr. Brian Burns (GE Healthcare) for the implementation of MP2RAGE acquisition pulse sequence on the MR950 scanner. GH is supported by Progetto di Attività Integrate - PAI Project - granted by IMT School for Advanced Studies Lucca to LC. LC would like to thank Fondazione IRIS for support and funding.

Supplementary materials

Supplementary material associated with this article can be found, in the online version, at doi:10.1016/j.neuroimage.2021.118574.

References

Acosta-Cabronero, J., Cardenas-Blanco, A., Betts, M.J., Butryn, M., Valdes-Herrera, J.P., Galazky, I., Nestor, P.J., 2017. The whole-brain pattern of magnetic susceptibility perturbations in Parkinson's disease. Brain 140, 118–131. doi:10.1093/brain/aww278.

Acosta-Cabronero, J., Williams, G.B., Cardenas-Blanco, A., Arnold, R.J., Lupson, V., Nestor, P.J., 2013. *In vivo* Quantitative Susceptibility Mapping (QSM) in Alzheimer's disease. PLoS ONE 8, e81093. doi:10.1371/journal.pone.0081093.

Argyridis, I., Li, W., Johnson, G.A., Liu, C., 2013. Quantitative magnetic susceptibility of the developing mouse brain reveals microstructural changes in the white matter. Neuroimage 88C, 134–142. doi:10.1016/j.neuroimage.2013.11.026.

Balla, D.Z., Sanchez-Panchuelo, R.M., Wharton, S.J., Hagberg, G.E., Scheffler, K., Francis, S.T., Bowtell, R., 2014. Functional quantitative susceptibility mapping (fQSM). Neuroimage 100, 112–124. doi:10.1016/j.neuroimage.2014.06.011.

Bianciardi, M., van Gelderen, P., Duyn, J.H., 2014. Investigation of BOLD fMRI resonance frequency shifts and quantitative susceptibility changes at 7 T. Hum. Brain Mapp. 35, 2191–2205. doi:10.1002/hbm.22320.

Biondetti, E., Karsa, A., David, Thomas, L., Shmueli, K., 2020. Investigating the accuracy and precision of TE-dependent versus multi-echo QSM using Laplacian-based methods at 3 T. Magn. Reson. Med. 84, 3040–3053. doi:10.1002/mrm.28331.

Brewer, A.A., Barton, B., 2016. Maps of the auditory Cortex. Annu. Rev. Neurosci. 39, 385–407. doi:10.1146/annurev-neuro-070815-014045.

Chen, W., Zhu, W., Kovanlikaya, Ii., Kovanlikaya, A., Liu, T., Wang, S., Salustri, C., Wang, Y., 2014. Intracranial calcifications and hemorrhages: characterization with Quantitative Susceptibility Mapping. Radiology 270, 496–505. doi:10.1148/radiol.13122640.

Chen, Z., Calhoun, V., 2015. Intrinsic functional brain mapping in reconstructed 4D magnetic susceptibility (χ) data space. J. Neurosci. Methods 241, 85–93. doi:10.1016/j.jneumeth.2014.12.014.

Chen, Z., Liu, J., Calhoun, V.D., 2013. Susceptibility-based functional brain mapping by 3D deconvolution of an MR-phase activation map. J. Neurosci. Methods 216, 33–42. doi:10.1016/j.jneumeth.2013.03.003.

Costagli, M., Donatelli, G., Biagi, L., Caldarazzo Ienco, E., Siciliano, G., Tosetti, M., Cosottini, M., 2016. Magnetic susceptibility in the deep layers of the primary motor cortex in amyotrophic lateral sclerosis. NeuroImage Clin. 12, 965–969. doi:10.1016/j.nicl.2016.04.011.

Costagli, M., Lancione, M., Cecchetti, L., Pietrini, P., Cosottini, M., Ricciardi, E., Tosetti, M., 2019. Quantitative Susceptibility Mapping of brain function during auditory stimulation. IEEE Trans. Radiat. Plasma Med. Sci. doi:10.1109/TRPMS.2019.2894262, 1–1.

Cox, R.W., 1996. AFNI: software for analysis and visualization of functional magnetic resonance neuroimages. Comput. Biomed. Res. 29, 162–173. doi:10.1006/CBMR.1996.0014.

Cronin, M.J., Wang, N., Decker, K.S., Wei, H., Zhu, W.-.Z., Liu, C., 2017. Exploring the origins of echo-time-dependent quantitative susceptibility mapping (QSM) measurements in healthy tissue and cerebral microbleeds. Neuroimage 149, 98–113. doi:10.1016/j.neuroimage.2017.01.053.

Da Costa, S., Saenz, M., Clarke, S., van der Zwaag, W., 2015. Tonotopic gradients in human primary auditory cortex: concurring evidence from high-resolution 7 T and 3 T fMRI. Brain Topogr. 28, 66–69. doi:10.1007/s10548-014-0388-0.

Da Costa, S., van der Zwaag, W., Marques, J.P., Frackowiak, R.S.J., Clarke, S., Saenz, M., 2011. Human primary auditory cortex follows the shape of Heschl's gyrus. J. Neurosci. 31, 14067–14075. doi:10.1523/JNEUROSCI.2000-11.2011.

de Rochefort, L., Liu, T., Kressler, B., Liu, J., Spincemaille, P., Lebon, V., Wu, J., Wang, Y., 2010. Quantitative susceptibility map reconstruction from MR phase data using bayesian regularization: validation and application to brain imaging. Magn. Reson. Med. 63, 194–206. doi:10.1002/mrm.22187.

Deistung, A., Schäfer, A., Schweser, F., Biedermann, U., Turner, R., Reichenbach, J.R., 2013. Toward in vivo histology: a comparison of quantitative susceptibility mapping (QSM) with magnitude-, phase-, and R2*-imaging at ultra-high magnetic field strength. Neuroimage 65, 299–314. doi:10.1016/J.NEUROIMAGE.2012.09.055.

Deistung, A., Schweser, F., Reichenbach, J.R., 2016. Overview of quantitative susceptibility mapping. NMR Biomed. doi:10.1002/nbm.3569.

Dick, F., Tierney, A.T., Lutti, A., Josephs, O., Sereno, M.I., Weiskopf, N., 2012. *In vivo* functional and myeloarchitectonic mapping of human primary auditory areas. J. Neurosci. 32, 16095–16105. doi:10.1523/JNEUROSCI.1712-12.2012.

Donatelli, G., Caldarazzo Ienco, E., Costagli, M., Migaleddu, G., Cecchi, P., Siciliano, G., Cosottini, M., 2019. MRI cortical feature of bulbar impairment in patients with amyotrophic lateral sclerosis. NeuroImage Clin 24. doi:10.1016/j.nicl.2019.101934.

Dumoulin, S.O., Wandell, B.A., 2008. Population receptive field estimates in human visual cortex. Neuroimage 39, 647–660. doi:10.1016/j.neuroimage.2007.09.034.

Elkady, A.M., Sun, H., Wilman, A.H., 2016. Importance of extended spatial coverage for quantitative susceptibility mapping of iron-rich deep gray matter. Magn. Reson. Imaging 34, 574–578. doi:10.1016/J.MRI.2015.12.032.

Friston, K.J., Holmes, A.P., Worsley, K.J., Poline, J..P., Frith, C.D., Frackowiak, R.S.J., 1994. Statistical parametric maps in functional imaging: a general linear approach. Hum. Brain Mapp. 2, 189–210. doi:10.1002/hbm.460020402.

Gawryluk, J.R., Mazerolle, E.L., D'Arcy, R.C.N., 2014. Does functional MRI detect activation in white matter? A review of emerging evidence, issues, and future directions. Front. Neurosci. 8. doi:10.3389/fnins.2014.00239.

Haacke, E.M., Liu, S., Buch, S., Zheng, W., Wu, D., Ye, Y., 2015. Quantitative susceptibility mapping: current status and future directions. Magn. Reson. Imaging doi:10.1016/j.mri.2014.09.004.

Hernández-Torres, E., Kassner, N., Forkert, N.D., Wei, L., Wiggermann, V., Daemen, M., Machan, L., Traboulsee, A., Li, D., Rauscher, A., 2017. Anisotropic cerebral vascular architecture causes orientation dependency in cerebral blood flow and volume measured with dynamic susceptibility contrast magnetic resonance imaging. J. Cereb. Blood Flow Metab. 37, 1108–1119.

Humphries, C., Liebenthal, E., Binder, J.R., 2010. Tonotopic organization of human auditory cortex. Neuroimage 50, 1202–1211. doi:10.1016/j.neuroimage.2010.01.046.

Jenkinson, M., Beckmann, C.F., Behrens, T.E.J., Woolrich, M.W., Smith, S.M., 2012. FSL. Neuroimage 62, 782–790. doi:10.1016/j.neuroimage.2011.09.015.

Karsa, A., Punwani, S., Shmueli, K., Anita Karsa, C., 2018. The effect of low resolution and coverage on the accuracy of susceptibility mapping. Magn. Reson. Med. 1–16. doi:10.1002/mrm.27542.

Kriegeskorte, N., Mur, M., Bandettini, P., 2008. Representational similarity analysis - connecting the branches of systems neuroscience. Front. Syst. Neurosci. 2, 4. doi:10.3389/neuro.06.004.2008.

Lancione, M., Donatelli, G., Cecchi, P., Cosottini, M., Tosetti, M., Costagli, M., 2019. Echo-time dependency of quantitative susceptibility mapping reproducibility at different magnetic field strengths. Neuroimage 197, 557–564. doi:10.1016/j.neuroimage.2019.05.004.

Lancione, M., Tosetti, M., Donatelli, G., Cosottini, M., Costagli, M., 2017. The impact of white matter fiber orientation in single-acquisition quantitative susceptibility mapping. NMR Biomed. 30. doi:10.1002/nbm.3798.

Langers, D.R.M., Krumbholz, K., Bowtell, R.W., Hall, D.A., 2014. Neuroimaging paradigms for tonotopic mapping (I): the influence of sound stimulus type. Neuroimage 100, 650–662. doi:10.1016/j.neuroimage.2014.07.044.

Langkammer, C., Liu, T., Khalil, M., Enzinger, C., Jehna, M., Fuchs, S., Fazekas, F., Wang, Y., Ropele, S., 2013. Quantitative Susceptibility Mapping in multiple sclerosis. Radiology 267, 551–559. doi:10.1148/radiol.12120707.

Langkammer, C., Pirpamer, L., Seiler, S., Deistung, A., Schweser, F., Franthal, S., Homayoon, N., Katschnig-Winter, P., Koegl-Wallner, M., Pendl, T., Stoegerer, E.M., Wenzel, K., Fazekas, F., Ropele, S., Reichenbach, J.R., Schmidt, R., Schwingenschuh, P., 2016. Quantitative Susceptibility Mapping in parkinson's disease. PLoS ONE 11, e0162460. doi:10.1371/journal.pone.0162460.

Langkammer, C., Schweser, F., Krebs, N., Deistung, A., Goessler, W., Scheurer, E., Sommer, K., Reishofer, G., Yen, K., Fazekas, F., Ropele, S., Reichenbach, J.R., 2012. Quantitative susceptibility mapping (QSM) as a means to measure brain iron? A post mortem validation study. Neuroimage 62, 1593–1599. doi:10.1016/J.NEUROIMAGE.2012.05.049.

Li, M., Newton, A.T., Anderson, A.W., Ding, Z., Gore, J.C., 2019. Characterization of the hemodynamic response function in white matter tracts for event-related fMRI. Nat. Commun. 10, 1–11. doi:10.1038/s41467-019-09076-2.

Li, W., Wang, N., Yu, F., Han, H., Cao, W., Romero, R., Tantiwongkosi, B., Duong, T.Q., Liu, C., 2015. A method for estimating and removing streaking artifacts in quantitative susceptibility mapping. Neuroimage 108, 111–122. doi:10.1016/j.neuroimage.2014.12.043.

Li, W., Wu, B., Avram, A.V., Liu, C., 2012. Magnetic susceptibility anisotropy of human brain *in vivo* and its molecular underpinnings. Neuroimage 59, 2088–2097. doi:10.1016/j.neuroimage.2011.10.038.

Li, W., Wu, B., Liu, C., 2011. Quantitative susceptibility mapping of human brain reflects spatial variation in tissue composition. Neuroimage 55, 1645–1656. doi:10.1016/j.neuroimage.2010.11.088.

Liu, C., Li, W., Johnson, G.A., Wu, B., 2011. High-field (9.4T) MRI of brain dysmyelination by quantitative mapping of magnetic susceptibility. Neuroimage 56, 930–938. doi:10.1016/j.neuroimage.2011.02.024.

Liu, C., Li, W., Tong, K.A., Yeom, K.W., Kuzminski, S., 2015. Susceptibility-weighted imaging and quantitative susceptibility mapping in the brain. J. Magn. Reson. Imaging doi:10.1002/jmri.24768.

Logothetis, N.K., Pauls, J., Augath, M., Trinath, T., Oeltermann, A., 2001. Neurophysiological investigation of the basis of the fMRI signal. Nature 412, 150–157. doi:10.1038/35084005.

Lotfipour, A.K., Wharton, S., Schwarz, S.T., Gontu, V., Schäfer, A., Peters, A.M., Bowtell, R.W., Auer, D.P., Gowland, P.A., Bajaj, N.P.S., 2012. High resolution magnetic susceptibility mapping of the substantia nigra in Parkinson's disease. J. Magn. Reson. Imaging 35, 48–55. doi:10.1002/jmri.22752.

Marques, J.P., Kober, T., Krueger, G., van der Zwaag, W., Van de Moortele, P.F., Gruetter, R., 2010. MP2RAGE, a self bias-field corrected sequence for improved segmentation and T1-mapping at high field. Neuroimage 49, 1271–1281. doi:10.1016/j.neuroimage.2009.10.002.

Mazzucchi, S., Frosini, D., Costagli, M., Del Prete, E., Donatelli, G., Cecchi, P., Migaleddu, G., Bonuccelli, U., Ceravolo, R., Cosottini, M., 2019. Quantitative susceptibility mapping in atypical Parkinsonisms. NeuroImage Clin. 24, 101999. doi:10.1016/j.nicl.2019.101999.

Moerel, M., De Martino, F., Santoro, R., Ugurbil, K., Goebel, R., Yacoub, E., Formisano, E., 2013. Processing of natural sounds: characterization of multipeak spectral tuning in human auditory cortex. J. Neurosci. 33, 11888–11898. doi:10.1523/JNEUROSCI.5306-12.2013.

O'Callaghan, J., Holmes, H., Powell, N., Wells, J.A., Ismail, O., Harrison, I.F., Siow, B., Johnson, R., Ahmed, Z., Fisher, A., Meftah, S., O'Neill, M.J., Murray, T.K., Collins, E.C., Shmueli, K., Lythgoe, M.F., 2017. Tissue magnetic susceptibility mapping as a marker of tau pathology in Alzheimer's disease. Neuroimage 159, 334–345. doi:10.1016/j.neuroimage.2017.08.003.

Özbay, P.S., Warnock, G., Rossi, C., Kuhn, F., Akin, B., Pruessmann, K.P., Nanz, D., 2016. Probing neuronal activation by functional quantitative susceptibility mapping under a visual paradigm: a group level comparison with BOLD fMRI and PET. Neuroimage 137, 52–60. doi:10.1016/j.neuroimage.2016.05.013.

Penny, W., Friston, K., Ashburner, J., Kiebel, S., Nichols, T., 2011. Statistical Parametric Mapping: The Analysis of Functional Brain Images. Elsevier.

Reichenbach, J.R., Schweser, F., Serres, B., Deistung, A., 2015. Quantitative susceptibility mapping: concepts and applications. Clin. Neuroradiol. 25, 225–230. doi:10.1007/s00062-015-0432-9.

Ren, J., Xu, T., Wang, D., Li, M., Lin, Y., Schoeppe, F., Ramirez, J.S.B., Han, Y., Luan, G., Li, L., Liu, H., Ahveninen, J., 2021. Individual variability in functional organization of the human and monkey auditory cortex. Cereb. Cortex 31, 2450–2465. doi:10.1093/CERCOR/BHAA366.

Saenz, M., Langers, D.R.M., 2014. Tonotopic mapping of human auditory cortex. Hear. Res. doi:10.1016/j.heares.2013.07.016.

Schenck, J.F., 1996. The role of magnetic susceptibility in magnetic resonance imaging: MRI magnetic compatibility of the first and second kinds. Med. Phys. 23, 815–850. doi:10.1118/1.597854.

Schofield, M.A., Zhu, Y., 2003. Fast phase unwrapping algorithm for interferometric applications. Opt. Lett. 28, 1194–1196. doi:10.1364/OL.28.001194.

Schweser, F., Deistung, A., Lehr, B.W., Reichenbach, J.R., 2011. Quantitative imaging of intrinsic magnetic tissue properties using MRI signal phase: an approach to in vivo brain iron metabolism? Neuroimage 54, 2789–2807. doi:10.1016/j.neuroimage.2010.10.070.

Schweser, F., Deistung, A., Lehr, B.W., Reichenbach, J.R., 2010. Differentiation between diamagnetic and paramagnetic cerebral lesions based on magnetic susceptibility mapping. Med. Phys. 37, 5165–5178. doi:10.1118/1.3481505.

Shih, C.M., Lo, H.C., Hsieh, M.C., Chen, J.H., 2021. Functional Quantitative Susceptibility mapping (fQSM) of rat brain during flashing light stimulation. Neuroimage 117924. doi:10.1016/j.neuroimage.2021.117924.

Shmueli, K., de Zwart, J.A., van Gelderen, P., Li, T.Q., Dodd, S.J., Duyn, J.H., 2009. Magnetic susceptibility mapping of brain tissue *in vivo* using MRI phase data. Magn. Reson. Med. 62, 1510–1522. doi:10.1002/mrm.22135.

Sjöström, H., Granberg, T., Westman, E., Svenningsson, P., 2017. Quantitative susceptibility mapping differentiates between parkinsonian disorders. Park. Relat. Disord. 44, 51–57. doi:10.1016/j.parkreldis.2017.08.029.

Smith, S.M., 2002. Fast robust automated brain extraction. Hum. Brain Mapp. 17, 143–155. doi:10.1002/hbm.10062.

Sood, S., Urriola, J., Reutens, D., O'Brien, K., Bollmann, S., Barth, M., Vegh, V., 2017. Echo time-dependent quantitative susceptibility mapping contains information on tissue properties. Magn. Reson. Med. 77, 1946–1958. doi:10.1002/mrm.26281.

Sun, H., Klahr, A.C., Kate, M., Gioia, L.C., Emery, D.J., Butcher, K.S., Wilman, A.H., 2018. Quantitative susceptibility mapping for following intracranial hemorrhage. Radiology 288, 830–839. doi:10.1148/radiol.2018171918.

Sun, H., Seres, P., Wilman, A.H., 2016. Structural and functional quantitative susceptibility mapping from standard fMRI studies. NMR Biomed. doi:10.1002/nbm.3619.

Sun, H., Wilman, A.H., 2015. Quantitative susceptibility mapping using single-shot echo-planar imaging. Magn. Reson. Med. 73, 1932–1938. doi:10.1002/mrm.25316.

Thomas, J.M., Huber, E., Stecker, G.C., Boynton, G.M., Saenz, M., Fine, I., 2015. Population receptive field estimates of human auditory cortex. Neuroimage 105, 428–439. doi:10.1016/J.NEUROIMAGE.2014.10.060.

Walsh, D.O., Gmitro, A.F., Marcellin, M.W., 2000. Adaptive reconstruction of phased array MR imagery. Magn. Reson. Med. 43, 682–690 10.1002/(SICI)1522-2594(200005)43:5<682::AID−MRM10>3.0.CO;2-G.

Wang, Y., Liu, T., 2015. Quantitative susceptibility mapping (QSM): decoding MRI data for a tissue magnetic biomarker. Magn. Reson. Med. 73, 82–101. doi:10.1002/mrm.25358.

Watson, A.B., Pelli, D.G., 1983. Quest: a Bayesian adaptive psychometric method. Percept. Psychophys. 33, 113–120. doi:10.3758/BF03202828.

Wei, H., Zhang, Y., Gibbs, E., Chen, N.K., Wang, N., Liu, C., 2016. Joint 2D and 3D phase processing for quantitative susceptibility mapping: application to 2D echo-planar imaging. NMR Biomed. doi:10.1002/nbm.3501, n/a-n/a.

Wharton, S., Bowtell, R., 2015. Effects of white matter microstructure on phase and susceptibility maps. Magn. Reson. Med. 73, 1258–1269. doi:10.1002/mrm.25189.

Wisnieff, C., Ramanan, S., Olesik, J., Gauthier, S., Wang, Y., Pitt, D., 2015. Quantitative susceptibility mapping (QSM) of white matter multiple sclerosis lesions: interpreting positive susceptibility and the presence of iron. Magn. Reson. Med. 74, 564–570. doi:10.1002/mrm.25420.

Worsley, K.J., Friston, K.J., 1995. Analysis of fMRI time-series revisited-again. Neuroimage 2, 173–181. doi:10.1006/nimg.1995.1023.

Yacoub, E., Shmuel, A., Logothetis, N., Uğurbil, K., 2007. Robust detection of ocular dominance columns in humans using Hahn Spin Echo BOLD functional MRI at 7 Tesla. Neuroimage 37, 1161–1177. doi:10.1016/j.neuroimage.2007.05.020.

Zhang, Y., Gauthier, S.A., Gupta, A., Comunale, J., Chia-Yi Chiang, G., Zhou, D., Chen, W., Giambrone, A.E., Zhu, W., Wang, Y., 2016. Longitudinal change in magnetic susceptibility of new enhanced multiple sclerosis (MS) lesions measured on serial quantitative susceptibility mapping (QSM). J. Magn. Reson. Imaging 44, 426–432. doi:10.1002/jmri.25144.

Zhou, D., Cho, J., Zhang, J., Spincemaille, P., Wang, Y., 2017. Susceptibility underestimation in a high-susceptibility phantom: dependence on imaging resolution, magnitude contrast, and other parameters. Magn. Reson. Med. 78, 1080–1086. doi:10.1002/mrm.26475.

Zhu, X., Gao, Y., Liu, F., Crozier, S., Sun, H., 2021. Deep grey matter quantitative susceptibility mapping from small spatial coverages using deep learning. Z. Med. Phys. doi:10.1016/J.ZEMEDI.2021.06.004.

Zwicker, E., 1961. Subdivision of the audible frequency range into critical bands (Frequenzgruppen). J. Acoust. Soc. Am. 33. doi:10.1121/1.1908630, 248–248.